Hysteresis of the drag force of an intruder moving into a granular medium

Antoine Seguin

EPJ manuscript No.
(will be inserted by the editor)

Hysteresis of the drag force of an intruder moving into a granular medium

A. Seguin[1]
[1] Laboratoire FAST, Université Paris-Sud, CNRS, Université Paris-Saclay, F-91405, Orsay, France.

the date of receipt and acceptance should be inserted later

Abstract. We numerically investigate the force-displacement relation of a moving intruder initially at rest into a granular medium. Our model granular medium is composed of one layer of coplanar polydisperse spheres subjected to a gravity field. The interactions between the grains are modelled by Hertzian contacts to which a viscous damping is applied. Moving it horizontally and with alternating positive and negative velocity, we recover a hysteresis of the force-displacement curve. Considering that the flow is plastic as the yield strength has been reached, we describe the transient part of the flow around the intruder. We show that the drag stress increases as its distance to an ultimate drag stress σ_u with a typical deformation ε_c: the drag stress - strains curve appears to exponentially decay as it saturates to this ultimate drag stress. This protocol of deformation highlights that the deformation of the grains is negligible compared to the deformation of the packing, i.e. related to the irreversible displacements of grains allowing the intruder to pass through. Simultaneously, the lift force is constant on average during the displacement of the intruder. We then give the different scaling laws of the yield strength, this ultimate drag stress, the characteristic deformation of the packing and the lift stress. Finally, we recover the complete hysteresis cycle of the drag force around the intruder.

PACS. 45.70.-n Granular systems – 83.80.Fg Granular solids (rheology)

1 Introduction

The application of cyclic deformation has always been a powerful tool for material characterization of metals or plastics: it often reveals interesting mechanical properties that can be exploited industrially. For those materials that are not divided media, cyclic tests are used to characterize the fatigue or aging of these materials. These properties are useful for predicting the life of a product and therefore sizing a product. In practice, for metals, when a load is applied and the yield strength (or elastic limit) is reached, there is a plastic deformation. In order to perform a compression test or a triaxial shear test on a granular medium, it is often necessary to initially compress the granular material so that it acquires rigidity. This prestress increases the volume fraction so that the granular medium is in its solid phase. For example, imposing a vacuum in the tank results in a compressive load being applied. To reach the elastic limit and trigger plastic deformation to study granular flow, the most common test is the shear test [1–3]. The shear is applied through the deformation of cell containing the granular medium which does not ensure a homogeneous shear in the bulk of the granular medium [4,5]. Several numerical studies have already been developed to investigate the evolution of the microstructure of a dense granular material under homogeneous oscillating shear without gravity. For very small deformations, the mechanical properties of the packing (elastic moduli) depend on the properties of the grains but also on the packing fraction [6]. To go further, finite element simulations were performed with an interactive Hookean force between grains in order to characterize the evolution of the pressure in the medium with the the architecture of

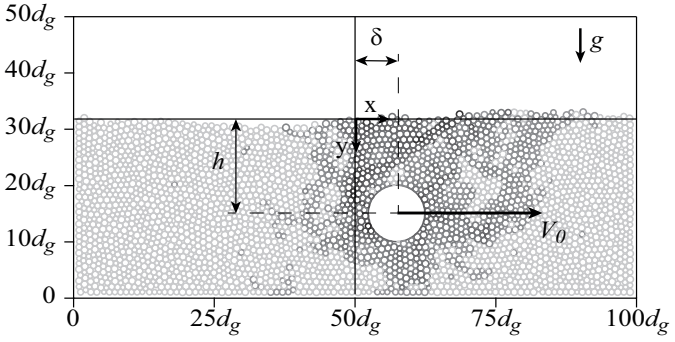

Fig. 1. Snapshot during displacement of the intruder at velocity V_0. The darkest grains have undergone a significant displacement during the intruder's displacement. The scales are in grain unit. The origin of the system of coordinates is defined as the middle of the cell in x direction and the average flat line in y direction. Thus the coordinates of the center of the intruder are defined with h vertically and δ horizontally.

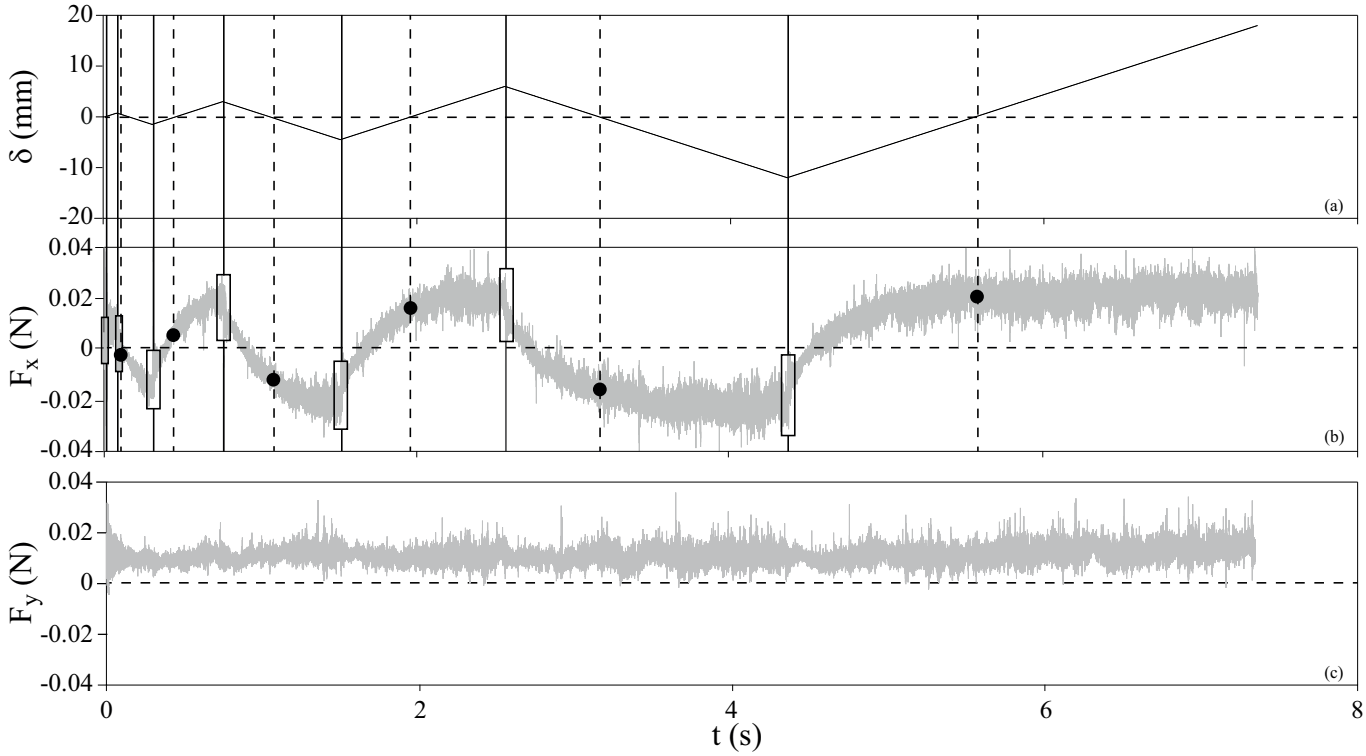

Fig. 2. Time evolution of **(a)** the position of a sphere δ moving into a granular medium, **(b)** the associated drag force F_x in the x direction and **(c)** the associated drag force F_y in the y direction. The sphere of diameter $d = 50d_g = 50$ mm embedded at $h = 100d_g = 100$ mm moves at velocity $V_0 = 10$ mm.s^{-1}. The horizontal dotted lines indicate zero value line of δ and F. The vertical dashed lines and the bullets indicate the existence of remaining drag force at $\delta = 0$. The vertical plain lines and the rectangular zone indicate the jump of the drag force which demonstrates the presence of a constant force threshold into the material.

the microstructure [7]. For dense packing, a hysteresis cycle in the stress-strain relationship was observed for oscillating shears [8]. In addition, experimental studies with a monodispersed granular medium have shown that the change in shear direction causes a sudden change in compactness [9]. The variations in the packing fraction within the material are correlated to the pressure and shear stress in the material [10]. Secondly, recent studies have highlighted non-local effects in granular medium leading to a more complex rheological law for granular medium and an inhomogeneous shear in the granular packing [11,12].

Unlike most studies that focus solely on steady flows, the goal of this paper is to characterize numerically the transient response of a granular medium around a moving object, from a state of rest to steady flow. Using a model granular medium consisting of one layer of coplanar spheres subjected to a field of gravity and constructing a drag stress - strain curve by horizontally moving an intruder back and forth through the granular packing. This motion creates a hysteresis cycle. With this local forcing, the drag stress response follows an exponential behavior with the displacement of the intruder while the lift stress remains independent of it. These behaviors are characterized by a typical deformation and an ultimate drag stress of the granular medium. We then give the different scaling laws of the yield strength, this ultimate drag stress, the characteristic deformation of the packing and the lift stress. We conclude by addressing several features of the plastic flow.

2 Numerical method and configuration

The present numerical setup is adapted from a previous configuration already used in [13]. A molecular dynamic method is used to perform two-dimensional simulations in the typical case illustrated in figure 1: an intruder is immersed in a granular medium and moved inside the medium. A circular intruder with a diameter d is initially buried in the granular medium at a depth h which represents the vertical distance (y-direction) from the upper surface of the granular medium to the center of the intruder (Fig. 1). This upper surface is defined as the average y-position of the grains constituting the last layer of grains in the initial state. The δ position of the intruder in the x-direction corresponds to the horizontal distance from the center of the tank to the center of the intruder such that $\delta = 0$ in the initial state (Fig. 1). To prepare for this initial state, the intruder was fixed in his initial buried position. Then, a diluted granular medium is placed above and its sedimentation under the action of gravity ($g = 9.81$ m.s^{-1} parallel to the y-direction) leads to the

initial configuration for further calculations. Once the sedimentation is complete, the tank filling level reaches a finite value that allows us to define h. The granular medium consists of spherical beads: we have chosen a uniform distribution from $0.8d_g$ to $1.2d_g$ in order to guarantee the absence of crystallization. In the following, we use only d_g as the average diameter of the beads. Each grain has a mass m and a Young's modulus E; we define the average density ρ based on the average diameter d_g. The tank containing the product is large enough that the lateral limits ($> 10d$) have no effect on the force exerted on the intruder by the grains [14]. This process leads to an average packag fraction of 0.83. This value is less than the critical volume fraction $\phi_J = 0.85$ indicating that the packing is rigid but still a loose packing [15,16]. In the following, our granular medium model is composed of spherical beads of density $\rho = 10^3$ kg.m^{-3} and effective Young's modulus $E = 1$ GPa. We use spherical beads of diameter d_g and therefore the effective length in the third direction is d_g, so the effective area of the intruder is dd_g. All grain interactions F_{ij} in the simulation are normal without tangential components. They are modelled with a dissipative Hertzian law of the form $F_{ij} = k\zeta^{3/2} - \lambda\frac{d\zeta}{dt}$ where ζ is the interpenetration of the grains, k is the stiffness of the contact and λ is a damping coefficient. The stiffness k is directly related to the mechanical property of the grains and also the diameter of the grain d_g through the relationship $k = E\sqrt{d_g/2}$. In order to dissipate energy during grain-to-grain contact, we decided to use a viscous damping λ in the grain contact law to reproduce a restitution coefficient $e_n = 0.9$ and to consider a zero microscopic coefficient of friction between grains. The interaction model differs from other numerical models that use linear contact laws with microscopic friction inducing tangential forces [6] or from much richer models in modeling energy dissipation during contacts [17]. In problems of grain flow around intruders, the existence of macroscopic friction, i. e. steric hindrance, makes it possible to capture physical phenomena [13]. The absence of microscopic friction between the grains does not prevent the local rheological laws of granular materials from being reproduced [18].

Once the initial configuration has been prepared, we move the intruder at constant speed V_0 along the x direction and 0 along the y-direction. During the movement of the intruder at constant speed V_0, we record the component of the force exerted by the granular medium on the intruder in the x-direction, called drag force F_x and in the y-direction called lift force F_y in the rest of the document. The time step is small enough to ensure numerical convergence. The details of these calculations were reported in [13]. In order to generate an independent velocity measurement, the macroscopic velocity time V_0 (d_g/V_0) must be longer than the microscopic grain rearrangement time related to the pressure created by the gravity field ($\sqrt{gd_g}$). It is the equivalent of imposing a Froude number $Fr = V_0/\sqrt{gd_g}$ smaller than 1. As part of our numerical configuration, it leads to the condition $V_0 \ll 0.1$ m.s^{-1} to ensure that the possible wake created behind the moving intruder is filled. It is also well established that for a small number of Froude, the evolution of the drag force is quasi static [19–23] and it is then useless to vary this parameter, so we keep V_0 constant at 10 mm.s^{-1} in all simulations. We then study the evolution of this drag force F according to the drag displacement δ of the intruder. We choose d_g as unit of length. We tune three parameters for all the simulations: the diameter d_g of the grains in the range $0.1 < d_g < 10$ mm, the depth h in the range $30d_g < h < 300d_g$ and the diameter d of the intruder in the range $20d_g < d < 100d_g$.

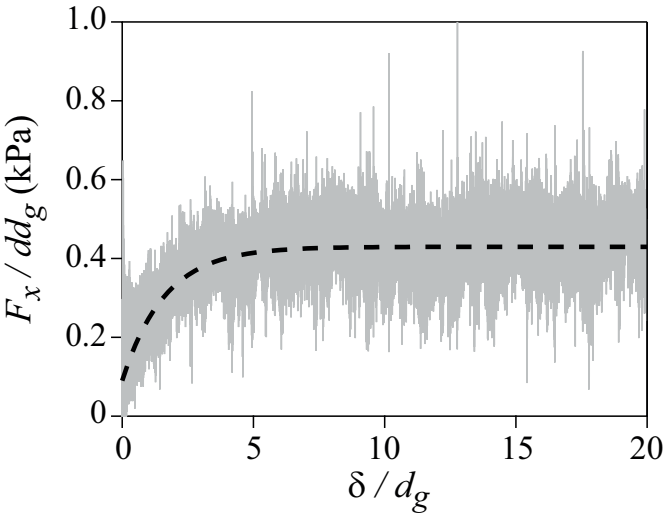

Fig. 3. Stress-strain curve $\sigma = F_x/dd_g$ as a function of $\varepsilon = \delta/d_g$ for $d = 50dg = 50$mm and $h = 100dg = 100$ mm. The dashed line (- -) is an exponential fit from Eq. 1 with $\sigma_u = 0.34$ kPa, $\sigma_Y = 0.09$ kPa and $\varepsilon_c = 1.6$.

3 Numerical results: Hysteresis cycle

A cyclic deformation is shown in figure 2. The position δ is plotted as a function of time on figure 2a while the constant speed V_0 of the intruder is imposed alternately positive or negative. The distance travelled by the intruder before switching increases arbitrarily over time. In summary, the intruder oscillates horizontally and the amplitude of these oscillations increases with each change of direction. We calculate the corresponding drag force F_x in the x-direction and it is displayed on the figure 2b. Even if the force presents strong fluctuations generated by the collisions between the intruder and the grains, we chose to keep the raw signal because the general behavior of the drag force F_x is always recognizable on the curve. We believe that these fluctuations contain information that is beyond the scope of this study: in this section, we consider only the evolution of the F_x average drag force on these fluctuations. First, the δ displacement is linear with time (Fig. 2a), since the speed is kept constant ($\pm V_0$). The drag force F_x increases or decreases according to the sign of the speed V_0 (Fig. 2b) but the evolution is not linear in time contrary to the displacement δ. For a large displacement amplitude, the drag force F_x is saturated to a

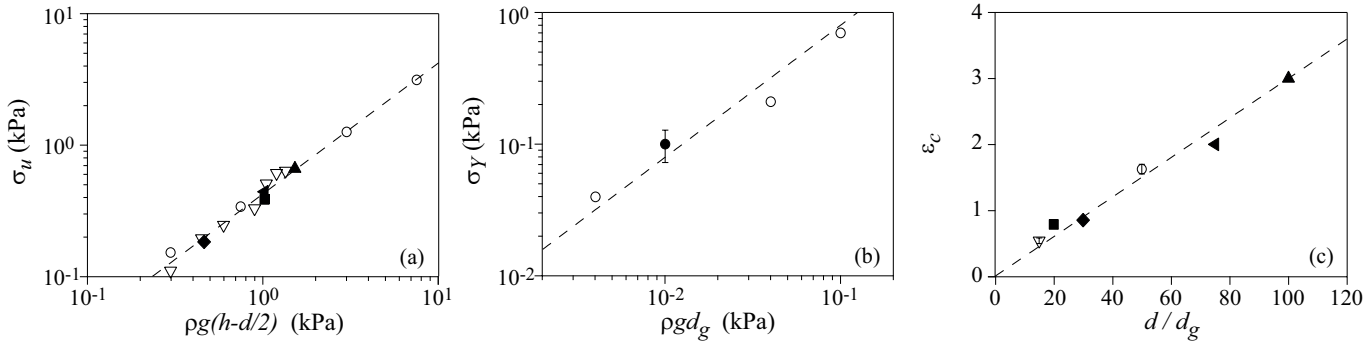

Fig. 4. (a) Ultimate stress σ_u as a function of hydrostatic pressure $\rho g(h-d/2)$. The symbols correspond to $d = 20d_g = 20$ mm (■), $d = 30d_g = 30$ mm (♦), $d = 75d_g = 75$ mm (◄), $d = 100d_g = 100$ mm (▲) and $d = 15d_g = 15$ mm (▽). The symbol (○) corresponds to $d = 50d_g$ and $h = 100d_g$ since d_g is the parameter that is varied for this symbol.**(b)** Yield strength σ_Y as a function of hydrostatic pressure $\rho g d_g$. The symbol (○) corresponds to $d = 50d_g$ and $h = 100d_g$ and the symbol (●) corresponds to corresponds to the average of all data obtained for $d_g = 1$mm. **(c)** Characteristic deformation ε_c as a function of the aspect ratio d/d_g. The symbols correspond to $d/d_g = 20$ (■), $d/d_g = 30$ (♦), $d/d_g = 75$ (◄), $d/d_g = 100$ mm (▲). The symbol (▽) and (○) corresponds to the average of all data obtained for $d/d_g = 15$ and $d/d_g = 50$ respectively. Dashed lines correspond to (a) $\sigma_u = \alpha\rho g(h-d/2)$ with $\alpha = 0.42 \pm 0.01$, (b) $\sigma_Y = \beta\rho g d_g$ with $\beta = 8 \pm 1$ and (c) $\varepsilon_c = \lambda d/d_g$ with $\lambda = 0.03 \pm 0.003$.

plateau value. This plateau value is symmetric for positive and negative drag forces. Secondly, we can see that there is no elastic deformation in the granular medium: there is always a non-zero F_x when $\delta = 0$ even if the saturated regime has not been reached (indicated by bullets in figure 2b). Third, during the speed sign change V_0 (indicated by vertical plain lines in figure 2b), there is a jump of the drag force (indicated by rectangles in figure 2b). This jump is visible in the discontinuity of the tangents of $F_x(t)$ on either side of a rectangle. These tangents do not touch during the change in sign of speed: this indicates the presence of a constant force threshold into the material. This jump can be interpreted as the elastic limit of the packing (or elastic limit σ_Y) that must be crossed twice to change direction of deformation. This elastic limit σ_Y corresponds to the minimum stress that must be applied to move the intruder. Thus, the deformation of the granular medium is mainly plastic. We note that this behavior is different from the nature of the grains in our simulation that have a finite modulus E and no yield strength [13]. As a result, in our experiment, the granular packing could be modeled as a solid with an infinite Young's modulus and a finite yield strength σ_Y. In summary, the elastic deformation of the stack is negligible compared to the plastic deformation and the elasticity of the grains is not relevant to study the deformation process of the packing. Although each grain has elastic behavior, the deformation ε in the entire medium is plastic. Moreover, we can see that the yield strength σ_Y does not increase with the amplitude of the cycles. These hysteresis cycle figures have been observed through simple or pure shear experiments on soil materials [8] but also on numerical simulations of sheared granular materials [7]. However, these studies are conducted in the solid phase of the granular material and require an initially very dense medium with a large volume fraction or a confining pressure ensuring the rigidity of the material. Here, in our simulations, there is no external confining pressure except that provided by gravity. We also notice that microscopic friction is not necessary and that we can use a Hertz contact model. In addition, the granular material is initially well-below the critical volume fraction and is loose. Figure 2c displays the evolution of the lift force F_y exerted by the granular material on the intruder. Several studies have already shown this lift force [17,24,25]. This lift force F_y is not negligible and is on average constant: it does not present hysteresis cycles at all unlike drag force. In the following, we will specify the behavior of this force-displacement curve and give the scaling laws of drag and lift forces.

4 Continuum description of the results

In this section, we describe the evolution of the force-displacement curve of the intruder. Here, we make a simple move in the x-direction (Fig. 1). By defining the drag stress on the intruder with the relationship $\sigma = F_x/dd_g$ and the normalized displacement as $\varepsilon = \delta/d_g$, it is possible to construct the typical drag stress-deformation curve (Fig. 3). Note that the drag stress defines a force per unit surface in order to get a parameter homogeneous to a pressure. In figure 2b, the drag stress σ increases roughly linearly from a non-zero value to values below ε and reaches a plateau at values above ε. This behaviour is similar to an exponential curve and can therefore be modelled using an equation of the form

$$\sigma = \sigma_Y + \sigma_u \left(1 - e^{-\frac{\varepsilon}{\varepsilon_c}}\right), \qquad (1)$$

where ε_c, σ_u and σ_Y are three parameters characterizing the granular packing. ε_c is a characteristic drag deformation of the packing. σ_u is the ultimate drag stress. σ_Y is the yield strength : as previously defined, it corresponds to the minimum stress that must be applied to move the

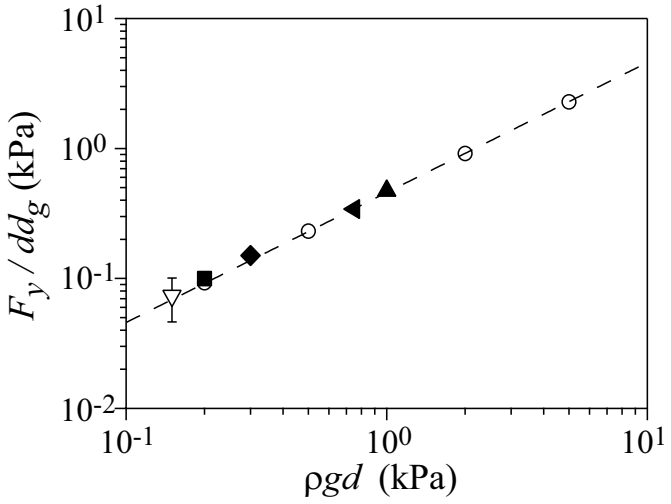

Fig. 5. Lift force per unit surface $\sigma_y = F_y/dd_g$ as a function of pressure ρgd (same symbols as in Fig. 4). Dashed line corresponds to $\sigma_y = \gamma \rho gd$ with $\gamma = 0.46 \pm 0.01$.

intruder. We notice that the asymptotic value reached by drag stress σ is $\sigma_Y + \sigma_u$ at large values of ε. A fit of the data was carried out on the case of figure 3 in order to determine the scaling laws of these three material parameters. This equation means that the stress excess from yield stress $\sigma - \sigma_Y$ increases as its distance to the ultimate stress σ_u with a characteristic length ε_c,

$$\varepsilon_c \frac{d(\sigma - \sigma_Y)}{d\varepsilon} = \sigma_u - (\sigma - \sigma_Y). \qquad (2)$$

A similar work can be performed by constructing a lift stress $\sigma_y = F_y/dd_g$ associated to the normalized displacement $\varepsilon = \delta/d_g$. It is possible to construct the typical lift stress-deformation curve (not shown as it is on average constant and comparable to figure 2c).

5 Scaling laws

In order to obtain the scaling laws of the material parameters, we fit each drag stress - strain curve obtained for different values of burial depth h, diameter d and grain diameter d_g with Eq. 1 (Fig. 3). Then we extract the three material parameters: characteristic deformation ε_c, yield strength σ_Y et ultimate stress σ_u. The influence of the burial depth h, diameter d and grain diameter d_g is shown in the figure 4 for the drag stress σ and in the figure 5 for the lift stress σ_y.

Spurious effects of a partial intruder immersion can be avoided by choosing h larger than the diameter of the intruder $h > d$. To avoid spurious effects of the bottom wall, h is also chosen far from the bottom of the tank, which means that the distance between the intruder's position and the bottom must be greater than d [14]. We observe that σ_Y and ε_c are rather constant with h (not shown but represented by the small amplitude of the standard deviations in figures 4b and 4c). The ultimate stress σ_u increases linearly with $h - d/2$. The presence of d/2 in this behavior comes from the geometry of the intruder. As the intruder is identified by the burial depth h of its center relative to the free surface. This means that $h = 0$ corresponds to an intruder halfway down, i. e. there is always one half $d/2$ of the intruder immersed in the packing (bottom half). In this situation, there is a non-zero drag force when the intruder moves. If the intruder is initially positioned at depth $h - d/2$, it is not in contact with the packing at all, the drag force is indeed zero in this case. The intruder that must be deep enough in the packing. We can see that the ultimate stress σ_u is more significant that the yield strength σ_Y especially at large depth h where σ_Y can be considered negligible comparated to σ_u.

The yield strength σ_Y does not depend on d (Fig. 4b) while the ultimate stress σ_u displays a small dependence (Fig. 4a). Finally, the scale of σ_u is similar to a hydrostatic pressure due to the weight of the column of grains above the intruder such as $\sigma_u \sim \rho g(h - d/2)$ (Fig. 4a). This means that in the limit case where $d/h << 1$, the size of the intruder does not affect this ultimate stress since $\sigma_u \sim \rho gh$. The scaling for the ultimate stress σ_u has been reported in many studies as corresponding to an established stationary flow [26–30,24]. Furthermore, it is also used in the construction of the inertial number I for granular flow under gravity [3]. The main influence of d is included in ε_c leading to $\varepsilon_c \sim d/d_g$ (Fig. 4c). The existence and scale of ε_c can be related to the localization of the velocity field (as it is related to the stress) in a granular flow around obstacles. It has been reported in previous studies [28,30,31].

Although the ultimate drag stress σ_u does not change with d_g (Fig. 4a), the yield strength σ_Y is proportionnal to the scale $\sigma_Y \sim \rho g d_g$ (Fig. 4b). This stress scale corresponds to the energy needed to move one grain on its own size. Therefore, the ratio σ_Y/σ_u only depends on h, d and d_g; it follows $\sigma_Y/\sigma_u = \gamma d_g/(h - d/2)$ with $\gamma \simeq 19$ using prefactorial values determined with the data (Fig. 4). The appearance of the yield strength in this case was not expected here and it cannot be neglected to describe the data. Several studies [32–35] investigate the yield strength using a pressure controlled setup (or a local force imposed via an intruder inside the packing) requiring a large compression of the granular packing. Moreover initial prestress might screen this yield stress and provide direct access to the ultimate stress. Figure 5 shows the evolution of the lift stress σ_y for all the simulations performed. The natural scale that emerges is $\sigma_y \sim \rho gd$, leading to $F_y \sim \rho g d^2 d_g$. Since $d^2 d_g$ is comparable to the intruder's volume, it means that the lift force is Archimedean in this problem. Thus, the deeper the intruder is buried, the more negligible this force will be in front of the drag force. In our numerical setup, we capture the transient part of the granular flow: from rest to flow.

6 Normalized cyclic deformation

We now derive the complete cyclic deformation from the drag stress-strain curve in figure 2. First we normalize the drag stress with the ultimate drag stress σ_u and the drag strain with the characteristic deformation ε_c. So considering the initial load defining the cycle 0, the stress $\sigma^{(0)}$ evolves according to the deformation $\varepsilon^{(0)}$, Eq. 1 can be rewritten as follows:

$$\frac{\sigma^{(0)}}{\sigma_u} = \frac{\sigma_Y}{\sigma_u} + \left(1 - e^{-\frac{\varepsilon^{(0)}}{\varepsilon_c}}\right). \quad (3)$$

In this initial cycle, using Eq. 3, $\varepsilon^{(0)}$ increases (with $d\varepsilon^{(0)} > 0$) from 0 to the final value $\varepsilon_f^{(0)}$ so that the intruder reaches the state $(\varepsilon_f^{(0)}/\varepsilon_c, \sigma_f^{(0)}/\sigma_u)$. For each subsequent cycle $2n$ with $d\varepsilon^{(2n)} > 0$, the intruder reaches the state $(\varepsilon_f^{(2n)}/\varepsilon_c, \sigma_f^{(2n)}/\sigma_u)$. The next cycle $2n+1$ corresponds to a reverse load (with $d\varepsilon^{(2n+1)} < 0$) and the intruder reaches the state $(\varepsilon_f^{(2n+1)}/\varepsilon_c, \sigma_f^{(2n+1)}/\sigma_u)$. Each end state is the starting point for the next cycle. So, more generally, each cycle $2n$ (with $d\varepsilon^{(2n)} > 0$) can be described by the general formula

$$\frac{\sigma^{(2n)}}{\sigma_u} = 1 + \frac{\sigma_Y}{\sigma_u} + \left(-1 + \frac{\sigma_f^{(2n-1)}}{\sigma_u}\right) e^{-\frac{\varepsilon^{(2n)} - \varepsilon_f^{(2n-1)}}{\varepsilon_c}}. \quad (4)$$

Similarly, each reverse load $2n+1$ (with $d\varepsilon^{(2n+1)} > 0$) can be described by the general formula

$$\frac{\sigma^{(2n+1)}}{\sigma_u} = -1 - \frac{\sigma_Y}{\sigma_u} + \left(1 + \frac{\sigma_f^{(2n)}}{\sigma_u}\right) e^{\frac{\varepsilon^{(2n+1)} - \varepsilon_f^{(2n)}}{\varepsilon_c}}. \quad (5)$$

This model recovers that the threshold σ_Y has to be crossed when there is a change in the sign of $d\varepsilon$. From eq. 3 corresponding to the initial load, eq. 4 corresponding to the load and eq. 5 corresponding to the reverse load, it is possible to build the complete cyclic drag stress - drag strain curve (Fig. 6) from the data of figure 2. The raw data have been filtered to allow a more direct comparison to the model. We note that there is no adjustable parameter in this curve, since λ, σ_u and σ_Y have been defined with the scaling laws of figure 4. Nevertheless the values of the initial state $(\sigma_f^{(n-1)}/\sigma_u, \varepsilon_f^{(n-1)}/\varepsilon_c)$ were released to perform the fit of the data. The original asymmetry of the cycle fades as the deformation increases. The succession of cycles conveys the mean value of the stress to zero. There are two sources of hysteresis in this cycle. The first source is generated by the yield strength σ_Y that exists at each change in the intruder's direction. This is reflected by the vertical slope in the modeled cycle in figure 6. The other source is generated by exponential behavior up to $\pm\sigma_u$ which is not reversible. However we notice that there is a small disparity between the model and the numerical data. This disparity may come from the preparation of a granular medium: the initial packing is rather loose. Through many cycles, the local packing fraction may increase a little and thus modify the drag stress - strain curve, as it has already been shown in other more complete rheological models [7]. Although the increase of the packing fraction is small, its influence on characteristic deformation could be significant, especially when approaching the jamming point. This effect has been reported in several studies [36, 21, 18] and is not taken into account in our model.

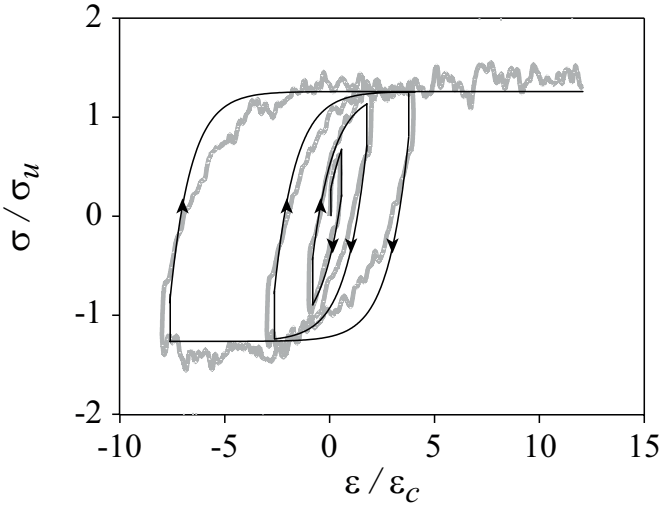

Fig. 6. Normalized stress σ/σ_u as a function of normalized deformation $\varepsilon/\varepsilon_c$ (in gray). The data are the same as figure 2 but they were filtered by a median filter. The solid line is a analytical combination of initial load from Eq. 3, the reverses loads from Eq. 5 and the loads from Eq 4. Arrows indicate the carrying out direction of the cycles.

7 Conclusion and perspectives

We made a cyclic drag stress - strain curve of a 2D granular medium made of spheres under a gravity field. This curve was obtained by moving a spherical intruder perpendicular to the gravity field in the bulk of the granular medium. This protocol of deformation has highlighted that the deformation of the grains is irrelevant compared to the deformation of the whole granular medium and finally there is no elasticity of the packing although it presents a yield strength σ_Y: all the deformation ε is plastic. From this threshold σ_Y, the drag stress σ_x increases exponentially with the drag deformation ε with a characteristic deformation ε_c up to an ultimate stress σ_u. In the case where this intruder is deeply buried in the granular packing ($d/h << 1$), the ultimate stress scales mainly as hydrostatic pressure due to the weight of the column of grain above the intruder $\sigma_u \sim \rho g h$. The characteristic deformation scales as the aspect ratio $\varepsilon_c \sim d/d_g$. The yield strength σ_Y scales as the weight of one grain $\sigma_Y \sim \rho g d_g$.

The yield stress σ_Y differs from the ultimate stress σ_u. In granular flows around intruder, as velocity is imposed, studies evaluate the ultimate drag stress and not the yield stress [28,23,37]. Actually the yield strength prevails in the first moment of the deformation before the flow of the material. The path from the yield stress to the ultimate stress is exponential regarding the displacement of the intruder. Our results provide a quantitative description of the transient flow before the stationary granular (plastic) flow. Furthermore, the study of this plastic flow and this ultimate drag stress belongs to rheology: many models have already been developed [5,11,38,39].

Understanding the structure of this path in term of microscopic material properties, such as microscopic friction or restitution coefficient, gives a better assesment of the macroscopic properties. This transient plastic regime, from rest to flow, has to be linked to local plastic events in terms of statistical properties and spatial hererogeneities. Comparisons to other divided media like foam or emulsion will represent a step forward in this field of research.

8 Acknowledgments

The author is grateful to J.C. Géminard for fruitful discussion and the referee for carefully reading the manuscript.

References

1. M.P. O'Reilly, S.F. Brown, *Cyclic loading of soils* (Blackie, 1991)
2. D. Howell, R. Behringer, C. Veje, Physical Review Letters **82**(26), 5241 (1999)
3. G. MiDi, European Physical Journal E–Soft Matter **14**(4) (2004)
4. S.C. du Pont, R. Fischer, P. Gondret, B. Perrin, M. Rabaud, Physical review letters **94**(4), 048003 (2005)
5. P. Jop, Y. Forterre, O. Pouliquen, Nature **441**, 727 (2006)
6. C.S. Chang, A. Misra, S.S. Sundaram, Soil Dynamics and Earthquake Engineering **10**(4), 201 (1991)
7. J. Sun, S. Sundaresan, Journal of Fluid Mechanics **682**, 590 (2011)
8. N. Khalili, M. Habte, S. Valliappan, International journal for numerical methods in engineering **63**(14), 1939 (2005)
9. M. Nicolas, P. Duru, O. Pouliquen, The European Physical Journal E **3**(4), 309 (2000)
10. J. Zhang, T. Majmudar, A. Tordesillas, R. Behringer, Granular Matter **12**(2), 159 (2010)
11. M. Bouzid, M. Trulsson, P. Claudin, E. Clément, B. Andréotti, Phys. Rev. Lett. **111**, 238301 (2013)
12. M. Bouzid, A. Izzet, M. Trulsson, E. Clément, P. Claudin, B. Andreotti, Eur. Phys. J. E **38**(11), 125 (2015)
13. A. Seguin, Y. Bertho, P. Gondret, J. Crassous, EPL **88**, 44002 (2009)
14. A. Seguin, Y. Bertho, P. Gondret, Phys. Rev. E **78**, 010301 (2008)
15. C.S. O'Hern, S.A. Langer, A.J. Liu, S.R. Nagel, Physical Review Letters **88**(7), 075507 (2002)
16. C.S. O'Hern, L.E. Silbert, A.J. Liu, S.R. Nagel, Physical Review E **68**(1), 011306 (2003)
17. Y. Ding, N. Gravish, D.I. Goldman, Physical Review Letters **106**(2), 028001 (2011)
18. A. Seguin, A. Lefebvre-Lepot, S. Faure, P. Gondret, Eur. Phys. J. E **39**(6), 1 (2016)
19. Y. Takehara, S. Fujimoto, K. Okumura, EPL **92**, 44003 (2010)
20. J.E. Hilton, A. Tordesillas, Phys. Rev. E **88**, 062203 (2013)
21. Y. Takehara, K. Okumura, Phys. Rev. Lett. **112**(14), 148001 (2014)
22. T. Faug, The European Physical Journal E **38**(5), 1 (2015)
23. A. Seguin, C. Coulais, F. Martinez, Y. Bertho, P. Gondret, Phys. Rev. E **93**, 012904 (2016)
24. F. Guillard, Y. Forterre, O. Pouliquen, Phys. Rev. Lett. **110**, 138303 (2013)
25. F.Q. Potiguar, Y. Ding, Phys. Rev. E **88**, 012204 (2013)
26. I. Albert, J.G. Sample, A.J. Morss, S. Rajagopalan, A.L. Barabási, P. Schiffer, Phys. Rev. E **64**, 061303 (2001)
27. Z. Peng, X. Xu, K. Lu, M. Hou, Phys. Rev. E **80**, 021301 (2009)
28. A. Seguin, Y. Bertho, P. Gondret, J. Crassous, Phys. Rev. Lett. **107**, 048001 (2011)
29. D.J. Costantino, J. Bartell, K. Scheidler, P. Schiffer, Phys. Rev. E **83**, 011305 (2011)
30. A. Seguin, Y. Bertho, F. Martinez, J. Crassous, P. Gondret, Phys. Rev. E **87**, 012201 (2013)
31. M.B. Stone, R. Barry, D.P. Bernstein, M.D. Pelc, Y.K. Tsui, P. Schiffer, Phys. Rev. E **70**, 041301 (2004)
32. R. Candelier, O. Dauchot, Phys. Rev. Lett. **103**, 128001 (2009)
33. R. Candelier, O. Dauchot, Phys. Rev. E **81**, 011304 (2010)
34. A. Fiege, M. Grob, A. Zippelius, Granular Matter **14**(2), 247 (2012)
35. A. Le Bouil, A. Amon, J.C. Sangleboeuf, H. Orain, P. Bésuelle, G. Viggiani, P. Chasle, J. Crassous, Granular Matter **16**(1), 1 (2014)
36. J.R. de Bruyn, A.M. Walsh, Canadian Journal of Physics **82**(6), 439 (2004)
37. R. Albert, M.A. Pfeifer, A.L. Barabási, P. Schiffer, Phys. Rev. Lett. **82**, 205 (1999)
38. D.L. Henann, K. Kamrin, Phys. Rev. Lett. **113**, 178001 (2014)
39. D. Berzi, J.T. Jenkins, Soft Matter **11**, 4799 (2015)